Precipitating Solar Wind Hydrogen at Mars: Improved Calculations of the Backscatter and Albedo with MAVEN Observations

Z. Girazian[1], J. Halekas[1]

[1]Department of Physics and Astronomy, University of Iowa, Iowa City, IA, USA

Key Points:

- We present new calculations of the hydrogen backscatter and albedo using low altitude proton measurements from MAVEN.
- Our calculated penetrating and backscatter energy spectra are consistent with model predictions.
- In agreement with expected trends, the albedo decreases with solar wind speed and increases with solar zenith angle.

Corresponding author: Zach Girazian, zachary-girazian@uiowa.edu

Abstract

Outside the Martian bow shock, charge exchange between solar wind protons and exospheric hydrogen produces energetic neutral atoms (ENAs) that travel towards Mars at the solar wind velocity. The penetrating ENAs deposit most of their energy near 150 km, but a fraction of them undergo enough collisions to be scattered back to space, resulting in a hydrogen albedo. Some of the penetrating ENAs are converted into protons upon reaching the collisional upper atmosphere. These protons can be measured by the Mars Atmosphere and Volatile EvolutioN's Solar Wind Ion Analzyer (SWIA) during periapsis passes, providing information about the penetrating and backscatter populations. In this work, we perform the first detailed analysis of the backscatter and albedo using SWIA observations. We find that our calculated backscatter energy spectra are consistent with model predictions and that, as expected, the penetrating and backscatter particle fluxes increase with solar wind speed and decrease with solar zenith angle (SZA). We also find that the albedo, which has an average value of 0.20±0.16, decreases with solar wind speed and increases at high SZAs near the terminator.

1 Introduction

Outside the Martian bow shock, solar wind protons charge exchange with hydrogen atoms in the extended exosphere to produce a population of energetic neutral atoms (ENAs) that stream towards Mars. Traveling at the solar wind speed, and unhindered by electromagnetic fields, the hydrogen ENAs precipitate into the upper atmosphere. There, the ENAs interact with the atmosphere through a variety of collisional processes that result in energy deposition, excitation and ionization of atmospheric species (Kallio & Barabash, 2001), proton aurora (Deighan et al., 2018; Ritter et al., 2018; Hughes et al., 2019), and ENA electron attachment and stripping (Shematovich et al., 2011; Bisikalo et al., 2017). Through these collisional processes, the ENAs are scattered, and a small fraction of them undergo enough collisions to be reflected back to space (Kallio & Barabash, 2001; Wang et al., 2018). These reflected ENAs are called the backscatter.

The Neutral Particle Detectors on Mars Express provided the first direct observations of the penetrating and backscatter ENAs, well above the altitude where the upper atmosphere becomes highly collisional (Futaana et al., 2006; Gunell, Holmström, et al., 2006; Mura et al., 2008; Wang et al., 2013, 2014). Recently, the lower altitude orbit of the Mars Atmosphere and Volatile EvolutioN (MAVEN) spacecraft has enabled observations of the collisional products of the incoming ENAs down to ∼150 km, covering altitudes where ENAs deposit most of their energy. These observations include measurements of protons and H^- ions that are produced by electron stripping and attachment of the hydrogen ENAs, primarily through collisions with atmospheric CO_2 (Halekas, Lillis, et al., 2015). Initial studies of the proton measurements by MAVEN's Solar Wind Ion Analyzer (SWIA) have been used to monitor the solar wind (Halekas, Benna, et al., 2015; Halekas et al., 2017; Fowler et al., 2019), study the hydrogen exosphere (Halekas, 2017), and characterize the penetrating population (Halekas, Lillis, et al., 2015; Henderson, 2019).

Although Halekas, Lillis, et al. (2015) presented a preliminary analysis of the backscatter population, it was not the focus of their investigation. In this work, we present the first detailed analysis of the backscatter and albedo with low altitude SWIA observations. We develop a new method to calculate penetrating and backscatter energy spectra, penetrating and backscatter particle fluxes, and albedos. Then, we characterize how they vary with solar zenith angle (SZA) and solar wind speed.

2 Method

2.1 SWIA Observations

We use the low altitude proton observations from MAVEN SWIA obtained between 2015-2020 at dayside SZAs less than 90°. SWIA is an electrostatic analyzer that measures ion fluxes at energies between 25 eV and 25 KeV (Halekas, Taylor, et al., 2015). Although SWIA's primary science goal is to measure solar wind flows both upstream and around Mars (Halekas et al., 2017), the instrument remains active through all phases of MAVEN's 4.5 hr elliptical orbit. During dayside periapsis passes, SWIA observes the signature of penetrating protons as an anti-sunward beam with the same energy as the upstream solar wind (Halekas, Lillis, et al., 2015).

Throughout this work, we use the "Coarse-3D" data products that have 8 second time resolution, 15% energy resolution, and 22.5 × 22.5 angular resolution across the entire 360 × 90° field of view. The "Survey" (rather than "Archive") data products are used to ensure consistent energy resolution and to gain the best possible observational coverage (Halekas et al., 2017). We focus solely on observations below 200 km where the atmosphere is highly collisional to precipitating ENAs and SWIA is likely to observe penetrating protons (Halekas, Lillis, et al., 2015). We also neglect observations at energies below 100 eV, which can become anomalous at periapsis when the spacecraft is negatively charged.

To ensure that our results are not influenced by any potential crustal magnetic field affects (Bisikalo et al., 2018), we remove MAVEN orbits during which the spacecraft passed through a region of strong crustal magnetic field while it was below 200 km. Strong crustal fields are defined as those with a magnitude of at least 20 nT at 400 km (Morschhauser et al., 2014).

2.2 Extracting the Penetrating and Backscatter Populations

To isolate the penetrating and backscatter populations, we classify each SWIA look direction as either "upward" or "downward". Downward look directions detect ions that have a component of their velocity pointing towards the planet. Upward look directions detect ions that have a component of their velocity pointing away from the planet. Both of these directions are defined relative to the planetary surface at the time of observation, as illustrated in Figure 1.

At any given time, t, we classify each look direction relative to the surface normal – the unit vector that extends radially outward from the center of Mars and points directly to the spacecraft. The surface normal is $\hat{n}(t) = \frac{\vec{R}(t)}{|\vec{R}(t)|}$, where $\vec{R}(t)$ is MAVEN's location in Mars-Solar-Orbital (MSO) coordinates. The dot product between a look direction vector, $\hat{\ell}$, and the surface normal, $\hat{n}(t)$, determines how the look direction is classified. If $\hat{\ell}\cdot\hat{n}(t)$ is positive, we classify the look direction as upward. If $\hat{\ell}\cdot\hat{n}(t)$ is negative, we classify the look direction as downward. Given these definitions, SWIA's field of view is evenly split so that at any given time there are an equal number of upward and downward look directions.

To first order, the upper atmosphere of Mars is spherically symmetric and densities decrease exponentially with altitude. The downward direction, then, captures particles travelling deeper into the atmosphere towards larger neutral densities. This includes the narrow, anti-sunward beam of penetrating protons, and also penetrating protons that have been scattered to some degree. The upward direction captures the backscatter – particles travelling out of the atmosphere towards smaller neutral densities.

Our definitions of upward and downward are markedly different than the definitions used in Halekas, Lillis, et al. (2015). Instead of SWIA's field of view being split evenly

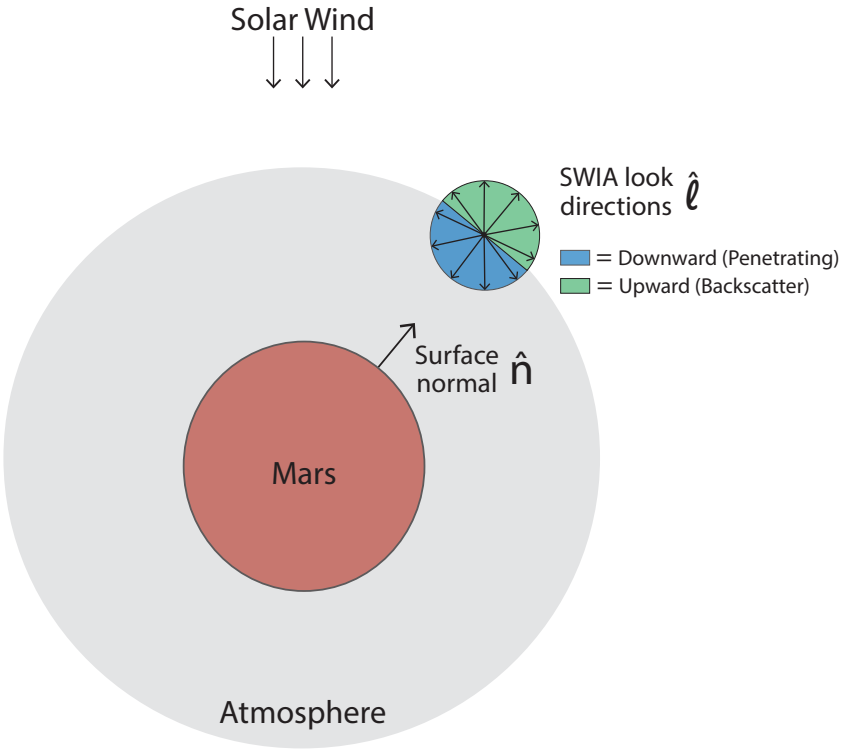

Figure 1. Schematic (not to scale) illustrating how we classify SWIA look directions as either "upward" or "downward" which we use to define the backscatter and penetrating populations, respectively.

between the upward and downward directions, they defined the downward field of view to include only look directions within 45° of anti-sunward, and the upward field of view to include all other look directions.

Figure 2a shows the time series of upward and downward angle-integrated spectra during a periapsis pass on 28 March 2015. As expected, penetrating protons are readily visible in the downward spectra below 200 km, appearing as a thin band of high flux at the solar wind energy ($\sim 10^3$ eV). Also consistent with expectations, penetrating protons are absent from the upward spectra which, upon close inspection, contain the backscatter population, appearing as a diffuse band of moderate flux below the solar wind energy.

Throughout our analysis, the solar wind energy is derived not from direct measurements, but from the peak energy of the orbit-averaged downward spectrum. To focus on times of quiet space weather, we restrict our analysis to times when the solar wind energy is between 540 eV and 1720 eV. This energy range corresponds to typical solar wind speeds at Mars (324 km s^{-1} to 578 km s^{-1}) (Halekas et al., 2017). If the peak energy of an orbit-averaged downward spectrum falls outside this energy range, we remove the orbit from our analysis.

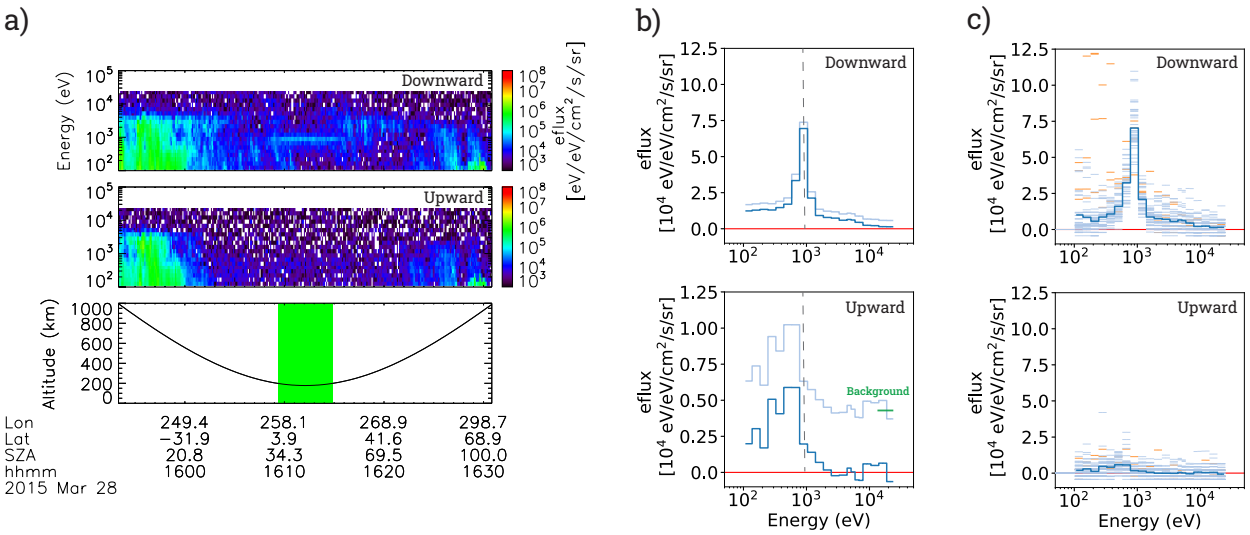

Figure 2. **a)** Time series of SWIA upward and downward angle-integrated differential energy spectra, and MAVEN's altitude, during a periapsis pass on 28 March 2015. The green rectangle highlights the observations used in our analysis (< 200 km). **b)** Orbit-averaged SWIA spectra before (light) and after (dark) background subtraction. The green line marks the background level, defined as the average flux in the four highest energy bins of the averaged upward spectrum. The vertical gray lines marks the solar wind energy. Note that the vertical axis of the upward spectrum is contracted for clarity. **c)** Every acceptable (light blue) and anomalous (orange) spectrum from the periapsis pass (<200 km). The dark blue lines show the orbit-averages after the anomalous spectra have been removed. The red lines in Panels b-c mark zero.

2.3 Background Subtraction

After the SWIA data is separated into upward and downward directions, we perform a procedure to subtract the instrumental background from each observation. The background is determined on an orbit-by-orbit basis since it likely remains stable during each periapsis pass. To calculate the background level during a single orbit, we first compute the orbit-averaged spectrum in the upward direction as shown in Figure 2b. The background is then defined as the average differential energy flux in the four highest energy bins (15-25 KeV) of this spectrum. Upward spectra are used to estimate the background because downward spectra often have higher fluxes or a secondary peak near these high energies, potentially due to the presence of precipitating pickup ions (Hara et al., 2017) or solar wind protons (Diéval et al., 2012, 2013).

Once the background level is computed, we subtract it from every flux measurement (before angle-averaging) from the orbit. Then, we recalculate the orbit-averaged upward and downward spectra using the background subtracted measurements. As demonstrated in Figure 2b, the background subtraction reduces fluxes at all energies and causes the high energy wings of the spectra to tend to zero. The background subtraction can also result in spectra having negative fluxes, which we do not attempt to correct.

Background levels throughout the dataset are on the order of $\sim 5 \times 10^3$ eV/(eV cm^2 s sr) but can increase dramatically during space weather events. The background level also steadily increased from (4.0×10^3 - 6.7×10^3) eV/(eV cm^2 s sr) between 2015-2020. This trend can be attributed to the steadily increasing galactic cosmic ray flux during the declining phase of Solar Cycle 24 (Ross & Chaplin, 2019).

2.4 Removing Anomalous Spectra

The orbit-averaged downward spectrum shown in Figure 2b has a narrow peak at the solar wind energy ($\sim 10^3$ eV), which is the hallmark signature of the proton population produced by precipitating solar wind ENAs. Other ion populations, however, may also be present in the SWIA observations. These include precipitating magnetosheath protons, (Diéval et al., 2012), precipitating pick-up ions (Hara et al., 2017), and precipitating hydrogen ENAs that originate in the magnetosheath (Gunell, Brinkfeldt, et al., 2006). Although it is difficult to completely separate these different populations, we perform a procedure to reduce their impact on our results. Our procedure eliminates observations from times when the downward energy spectrum has an absolute maximum far from the solar wind energy.

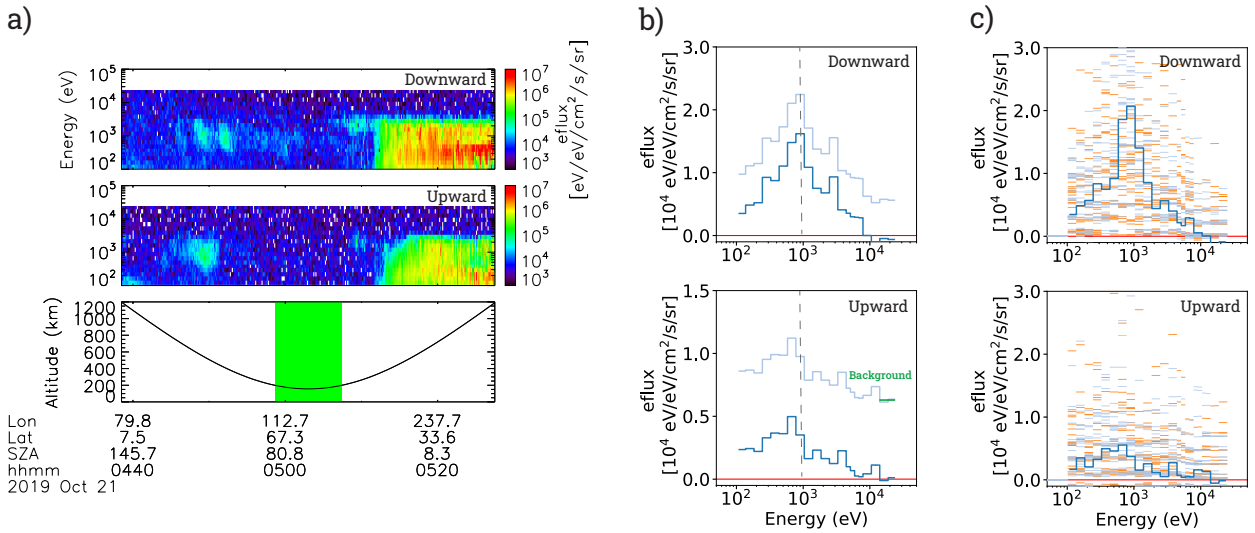

Figure 3. Same as Figure 2 but showing a periapsis pass on 21 October 2019 when the penetrating proton signal was weaker and more anomalous spectra were observed.

To demonstrate this procedure, Figure 2c shows every background subtracted energy spectrum from the 28 March 2016 orbit. Every blue spectrum has an absolute maximum within ±2 energy bins of the solar wind energy. Every orange spectrum has an absolute maximum at least two energy bins outside of the solar wind energy. Since the solar wind energy likely remains fixed for the ∼10 minutes MAVEN is below 200 km, we consider the orange spectra anomalous, and remove them from our analysis. After their removal, we recalculate the orbit-averaged spectra, which are shown with thick blue lines in Figure 2c. The removal of the four anomalous spectra during this orbit leads to smaller fluxes in the low energy wings of the recalculated orbit-averaged spectra.

During a typical orbit, SWIA obtains ∼60 spectra below 200 km. For an orbit to be included in our analysis, we require less than 50% of the spectra be anomalous. This requirement ensures that the orbits we use contain a clear penetrating proton signal. Although the threshold value of 50% is somewhat arbitrary, we chose it after inspecting a variety of threshold values, and it allows us to maintain enough orbits to have robust statistics.

When the penetrating proton signal is strong, such as during southern summer (Halekas, 2017), there are usually fewer anomalous spectra during a periapsis pass. Conversely, when the penetrating proton signal is weak, there are more anomalous spectra. An example

of a periapsis pass with a weak penetrating proton signal is shown in Figure 3. It contains nearly 50% anomalous spectra with 32 of the 66 downward spectra having a peak more than two energy bins outside the solar wind energy. The resulting orbit-averaged downward spectrum (Figure 3b) has a broader peak compared to the example shown in Fig. 2. After removing the 32 anomalous spectra, the recalculated orbit-averaged downward spectrum has a narrower peak (Figure 3c), as expected for penetrating protons.

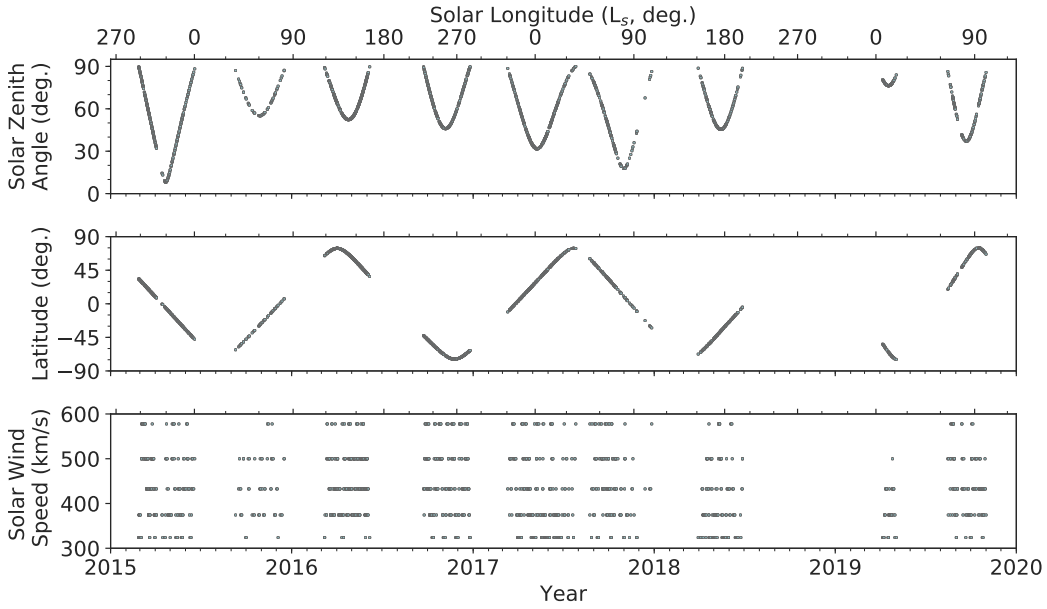

Figure 4. Observational coverage of the 1617 orbits used in our analysis showing solar zenith angle (top), latitude (middle), and solar wind speed (bottom).

2.5 Directional Fluxes and Albedo

For each orbit that we calculate orbit-averaged energy spectra, we also calculate orbit-averaged directional fluxes (cm^{-2} s^{-1}). The directional fluxes during a single orbit are calculated using the background-subtracted observations after removing observations from times when there was an anomalous spectrum. At each time during the orbit, the downward directional flux, F_{down} is defined as $F_{down} = -\vec{J}_{down}(t)\cdot\hat{n}(t)$, where $\vec{J}_{down}(t)$ is the particle flux derived from the three dimensional energy distribution in the downward direction. The negative sign forces $\vec{J}_{down}(t)$ to be a positive quantity. Similarly, the upward directional flux, F_{up}, is defined as $F_{up} = \vec{J}_{up}(t) \cdot \hat{n}(t)$, where $\vec{J}_{up}(t)$ is the particle flux derived from the three dimensional energy distribution in the upward direction. We then define the albedo as F_{down}/F_{up}, the ratio of the upward and downward directional fluxes.

2.6 Observational Coverage

After applying our method we are left with 1617 orbits SWIA data to analyze. Figure 4 shows the dates, solar longitudes (L$_s$), SZAs, latitudes, and solar wind speeds during these orbits. These parameters are assigned to the orbit-averaged quantities using their values at the time of MAVEN's periapsis during the orbit. The solar wind speed for each orbit is derived using $V_{sw} = (2E_{peak}/m_p)^{1/2}$, where V_{sw} is the solar wind speed, m_p is the proton mass, and E_{peak} is the peak energy of the orbit-averaged downward spec-

trum. In the next two sections we present our analysis of the energy spectra (Section 3), directional fluxes, and albedo (Section 4).

3 Results: Energy Spectra

3.1 Overview of Energy Spectra

Figure 5 shows the orbit-averaged upward and downward spectra from nine different orbits. All of the downward spectra have narrow peaks at the presumed solar wind energy, consistent with the penetrating proton population being produced primarily by ENAs that originate outside the bowshock in the pristine solar wind. The smaller fluxes observed outside the solar wind energy are produced by penetrating protons that have undergone multiple scatterings, though not enough to be reflected in the upward direction. A portion of the flux at these surrounding energies may also be produced by hydrogen ENAs produced in the magnetosheath, precipitating solar wind protons, or precipitating pick-up ions.

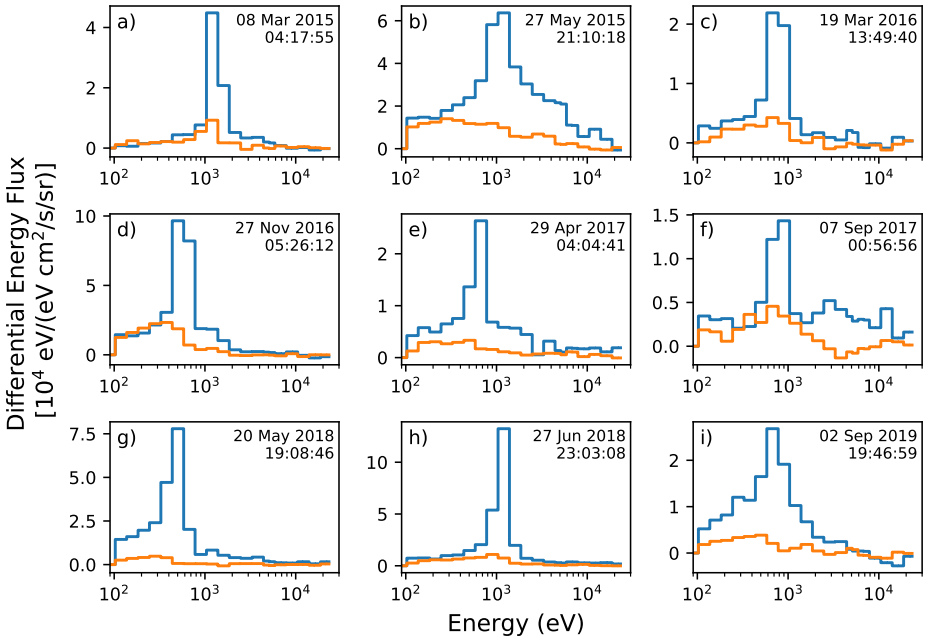

Figure 5. Examples of orbit-averaged differential energy spectra calculated using the method described in Section 2. Each panel shows the downward (blue) spectrum, representative of the penetrating proton population, and the upward (orange) spectrum, representative of the backscatter population. The date in each panel is the time of MAVEN's periapsis during the orbit.

Comparatively, the upward spectra have broader peaks near or below the solar wind energy. This is consistent with expectations for the the backscatter population, which is produced by penetrating protons that have lost energy after undergoing enough collisions to be backscattered (Kallio & Barabash, 2001; Bisikalo et al., 2018). In nearly every example, the upward spectra have smaller fluxes at all energies when compared to the downward spectra. This differs significantly from the backscatter spectra presented in Halekas, Lillis, et al. (2015), which could not be reproduced by the model of Bisikalo et al. (2018). In Halekas, Lillis, et al. (2015), the backscatter fluxes are larger than the

penetrating fluxes in the low and high energy wings surrounding the solar wind energy. This suggests that our method, which includes a robust background subtraction and uses different fields of view to define the penetrating and backscatter populations (Section 2.2), is an improvement.

3.2 Dependence on Solar Wind Speed

Figure 6a-b shows averages of the penetrating and backscatter differential energy spectra for five typical solar wind speeds. The averages were calculated using the complete ensemble of orbit-averaged spectra, which cover a wide range of SZAs and seasons for a given solar wind speed (Fig. 4). Compared to the penetrating spectra, the backscatter spectra have broader distributions and smaller peak energies. In every case, the peak energy of the backscatter spectrum is ∼75% smaller than the peak energy of the corresponding penetrating spectrum. These properties of the backscatter spectra are consistent with the expected energy depletion that accompanies numerous collisions (Kallio & Barabash, 2001; Bisikalo et al., 2018).

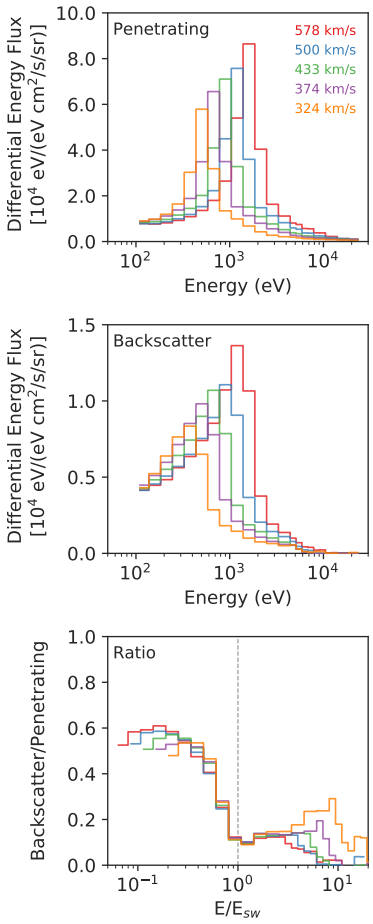

Figure 6. The top and middle panels show ensemble averages of the penetrating (downward) and backscatter (upward) differential energy spectra as a function of solar wind speed. The bottom panel shows the ratios of backscatter and penetrating spectra with the horizontal axis scaled relative to the solar wind energy. The vertical gray line marks the solar wind energy.

The differential fluxes in both the penetrating and backscatter spectra increase monotonically with increasing solar wind speed. This trend is consistent with previous results (Halekas, Lillis, et al., 2015) and can be explained by considering that both the H-H^+ charge exchange cross section, and the H-CO_2 electron stripping cross section, increase with solar wind speed (Kallio & Barabash, 2001). The H-H^+ charge exchange cross section controls the hydrogen ENA production rate in the solar wind, while the H-CO_2 electron stripping cross section controls the rate at which precipitating ENAs are converted into protons in the collisional upper atmosphere. Thus, both the precipitating ENA flux, and the fraction of ENAs converted into protons in the upper atmosphere, increase with solar wind speed.

3.3 Flux Ratios

Figure 6c shows the ratios of the backscatter and penetrating energy spectra for different solar wind speeds. The ratios are plotted as a function of E/E_{sw} where E is energy and E_{sw} is the solar wind energy. Across all solar wind speeds, the ratios are closely aligned between E/E_{peak} = 0.3 - 3.0. Since most of the flux resides in this energy range, this suggests that the ratios are only weakly dependent on solar wind energy.

The ratios are also less than one across all energies, which is in stark contrast to the results of Halekas, Lillis, et al. (2015), who found the ratio commonly exceeds one in the low and high energy wings. Our smaller ratios are more consistent with the model predictions of Bisikalo et al. (2018). In their Figure 5a, they show their predictions of the penetrating and backscatter energy spectra for precipitating hydrogen ENAs at 160 km. At energies well below the solar wind energy ($E/E_{peak} < 0.5$), they predict ratios between ∼1-5. Our calculated ratios in this energy region are smaller, ranging between 0.4-0.6. However, Figure 6a of Bisikalo et al. (2018) shows their predicted energy spectra if both precipitating hydrogen ENAs and precipitating magnetosheath protons are included. The inclusion of precipitating protons reduces their predicted flux ratios in the low energy range to ∼0.1-0.5, much closer to our calculated values. This likely indicates that our method is unable to completely remove the precipitating magnetosheath proton population from SWIA observations (Section 2.4).

At higher energies ($E/E_{peak} > 0.75$), the predicted backscatter spectra in Bisikalo et al. (2018) have a steep slope resulting in ratios of 0.01 or less in the high energy wing. Our backscatter spectra have a less steep slope resulting in ratios that are ∼10 times larger. Despite this discrepancy, our ratios in the high energy wing are smaller than one, which makes them more consistent with the model predictions compared to previous work (Halekas, Lillis, et al., 2015). The observed high energy ratios in Halekas, Lillis, et al. (2015), which often exceeded one, are larger because they used a much larger field of view to define the backscatter population (Section 2.2).

4 Results: Directional Fluxes and Albedo

4.1 Dependence on Solar Zenith Angle

Figure 7 (top) shows the penetrating and backscatter directional fluxes as a function of SZA. Although there is significant scatter in the orbit-averaged values, the SZA-binned medians decrease with increasing SZA. From SZA=15°-85°, the penetrating flux decreases by a factor ∼3.5 and the backscatter flux decreases by a factor of ∼2.0. The albedo, also shown in Figure 7 (bottom), has a constant median value of ∼0.15 between SZA=15°-65°, then increases to ∼0.25 near the terminator.

These SZA trends are consistent with expectations. Prior to being scattered, the penetrating ENAs travel in the solar wind direction which, at the subsolar point, is anti-parallel to the surface normal (Fig. 1). Thus, the entire ENA flux vector points in the

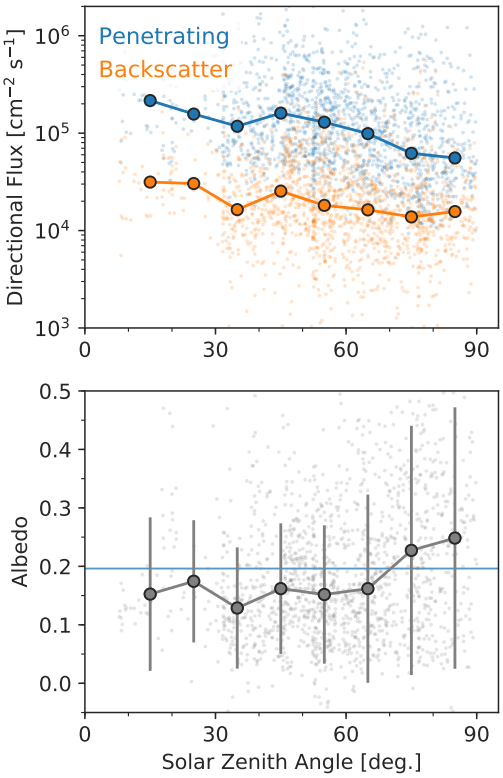

Figure 7. Directional fluxes (top) and albedo (bottom) as a function of solar zenith angle (SZA). The small circles are the orbit-averaged values. The large circles are the median values calculated using 10° SZA bins. The error bars in the albedo plot are the standard deviations in each SZA bin, and the blue line marks the mean albedo of the entire dataset (0.20).

downward direction. But at higher SZAs, there is an angle between the solar wind direction and the surface normal, so only a component of the ENA flux vector points in the downward direction. As this angle widens with increasing SZA, the penetrating flux decreases.

Since backscatter flux is also produced by the ENAs, it decreases similarly with SZA when far from the terminator. However, when close to the terminator, the backscatter flux decreases less drastically with SZA because it takes fewer collisions to reflect an ENA upward when there is a wider angle between solar wind and surface normal. Furthermore, as the solar wind incidence angle approaches grazing incidence, the penetrating ENAs must travel through a thicker column of atmosphere to reach thermospheric altitudes, resulting in more collisions and a higher albedo near the terminator.

We can compare our results to model predictions of the precipitating hydrogen ENA flux formed above the atmosphere in the solar wind. Near the subsolar point, models predict a penetrating ENA flux of $\sim (4.0-7.0)\times10^6$ cm^{-2}s^{-1} (Kallio & Barabash, 2001; Wang et al., 2018). Given that (4-15)% of the ENAs are expected to be converted into protons upon reaching the upper atmosphere (Halekas, 2017), this suggests that the penetrating proton flux observed by SWIA near the subsolar point should be $\sim (2.0-10.0)\times 10^5$ cm^{-2}s^{-1}, which is consistent with our results. Models also predict that between SZA=15°-85°, the precipitating ENA flux decreases by a factor of $\sim (6-9)$ (Kallio & Barabash, 2001; Wang et al., 2018). This is larger than the factor of 3.5 decrease we observe in the

penetrating flux. This discrepancy may be due to our imperfect removal of the precipitating magnetosheath proton population (Section 2.4), which has a weaker dependence on SZA compared to the solar wind ENA population (Wang et al., 2018).

4.2 Dependence on Solar Wind Speed

Figure 7 shows how the average penetrating flux (top), backscatter flux (middle), and albedo (bottom) vary with solar wind speed. The average value at each solar wind speed is computed using all of the orbit-averaged values that cover a wide range of seasons and SZAs. As expected, the penetrating and backscatter fluxes increase with solar wind speed due to the energy dependence of the H-H^+ charge exchange and H-CO_2 electron stripping cross sections (Sec. 3.2).

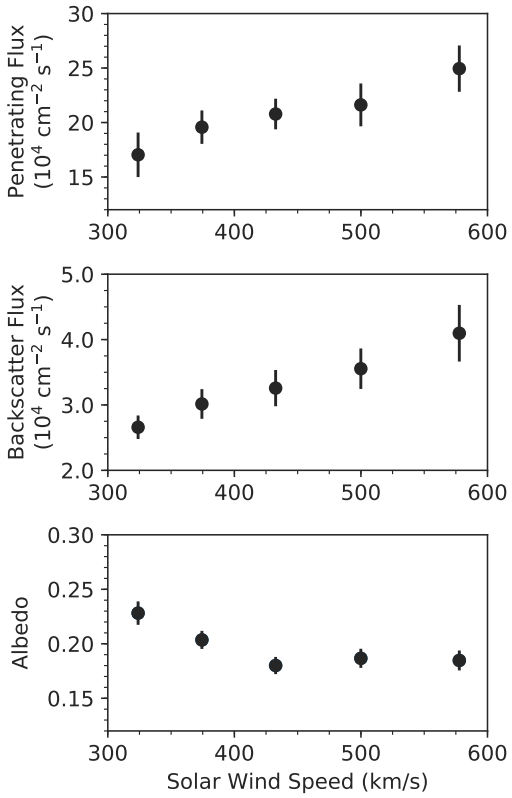

Figure 8. The penetrating flux (top), backscatter flux (middle), and albedo (bottom) as a function of solar wind speed. The circles are averages calculated using all of the orbit-averaged values from a given solar wind speed. The number of orbit-averaged values at each solar wind speed ranges from 179 to 439. The error bars are the standard error of the mean.

The albedo decreases by ∼20% with increasing solar wind speed, but the relationship is not strictly monotonic. It decreases from 0.23 at a solar wind speed of 324 km s^{-1}, to 0.18 at solar wind speeds of 433 km s^{-1} and greater. It is somewhat surprising that the albedo does not decrease monotonically with solar wind speed. A monotonic relationship might be expected given that the H-CO_2 elastic collisional cross section decreases with solar wind speed (Kallio & Barabash, 2001). Thus, as solar wind speed increases, there ought to be fewer elastic collisions and a smaller albedo. Determining why

the albedo varies in this manner may require modeling studies conducted under various solar wind conditions which, to our knowledge, do not currently exist.

5 Discussion

We have demonstrated that our method used to calculate penetrating and backscatter energy spectra improves upon previous work. In our spectra, the ratios between the backscatter and penetrating fluxes in the low and high energy wings are smaller than those presented in Halekas, Lillis, et al. (2015), making them more consistent with model predictions (Bisikalo et al., 2018). In Halekas, Lillis, et al. (2015), the ratios in the low and high energy tails are greater than one because they used a wider field of view to define the backscatter population. Future comparisons between our spectra and model predictions will allow for more accurate quantitative comparisons.

We have also shown how the directional fluxes and albedo vary with SZA and solar wind speed. The observed SZA trends are consistent with expectations; the penetrating and backscatter fluxes decrease with SZA and the albedo increases near the terminator as the the solar wind angle approaches grazing incidence with respect to the atmosphere. The observed trends with solar wind speed are also generally consistent with expectations. As solar wind speed increases, the penetrating and backscatter fluxes increase and the albedo decreases from 0.23 to 0.18. Somewhat surprisingly, however, the relationship between the albedo and solar wind speed is not strictly monotonic.

Using all of our observations, we find an average albedo of 0.20 ± 0.16, which is smaller than the $\sim$0.5 reported in Halekas, Lillis, et al. (2015). Model predictions of the albedo range between 0.15-0.58 (Kallio & Barabash, 2001; Shematovich et al., 2011; Wang et al., 2018), which is consistent with our results. However, a direct comparison between our calculated albedo and model predictions is not possible since SWIA only observes the proton population at low altitudes. Thus, the SWIA observations do not capture backscattered neutrals (Futaana et al., 2006) or particles reflected above 200 km. Moreover, the SWIA observations may underestimate the ENA albedo due to the relative energy dependence of the charge exchange and electron stripping cross sections, which causes the equilibrium proton fraction in the collisional atmosphere to decrease with energy (Halekas, Lillis, et al., 2015). Since the backscatter population has a lower average energy than the penetrating population, a smaller fraction of backscattered ENAs ought to be in charged form.

The orbit-averaged directional fluxes and albedo derived from SWIA observations exhibit substantial variability. Although we have explained some of this variability by considering solar wind speed and SZA, there are other factors that undoubtedly affect the ENA flux. (Halekas, 2017). These include transient space weather events, the bow shock standoff distance, and the seasonally varying exospheric hydrogen column density. Both crustal and induced magnetic fields are also expected to strongly affect the backscatter and albedo (Kallio et al., 2006; Wang et al., 2014; Shematovich et al., 2011; Bisikalo et al., 2018). Understanding the role of magnetic fields is an interesting avenue for future investigations.

6 Conclusions

We have presented the first detailed study of the ENA backscatter and albedo with low altitude SWIA observations. Future comparisons of our results with model predictions will improve our understanding of the processes that affect solar wind hydrogen deposition and backscatter at Mars.

Acknowledgments

This research was conducted under the support of the MAVEN mission which is funded by NASA headquarters. Support for J. Halekas was also provided by NASA grant NNX16A084G. We thank Nicholas Jones for providing useful insights. All of the MAVEN data used in this study are publicly available from the Planetary Data System (`https://pds-ppi.igpp.ucla.edu/search/?sc=MAVEN&t=Mars`). The calculated energy spectra and directional fluxes used in our analysis will be archived on `zenodo.org` upon acceptance of the manuscript.

References

Bisikalo, D. V., Shematovich, V. I., Gérard, J. C., & Hubert, B. (2017, January). Influence of the crustal magnetic field on the Mars aurora electron flux and UV brightness. *Icarus*, *282*, 127–135. Retrieved 2020-01-03, from `http://www.sciencedirect.com/science/article/pii/S0019103516305504` doi: 10.1016/j.icarus.2016.08.035

Bisikalo, D. V., Shematovich, V. I., Gérard, J.-C., & Hubert, B. (2018). Monte Carlo Simulations of the Interaction of Fast Proton and Hydrogen Atoms With the Martian Atmosphere and Comparison With In Situ Measurements. *Journal of Geophysical Research: Space Physics*, *123*(7), 5850–5861. Retrieved 2020-02-10, from `https://agupubs.onlinelibrary.wiley.com/doi/abs/10.1029/2018JA025400` doi: 10.1029/2018JA025400

Deighan, J., Jain, S. K., Chaffin, M. S., Fang, X., Halekas, J. S., Clarke, J. T., ... Jakosky, B. M. (2018, October). Discovery of a proton aurora at Mars. *Nature Astronomy*, *2*(10), 802–807. Retrieved 2019-12-04, from `http://www.nature.com/articles/s41550-018-0538-5` (tex.ids: deighanDiscoveryProtonAurora2018a) doi: 10.1038/s41550-018-0538-5

Diéval, C., Kallio, E., Barabash, S., Stenberg, G., Nilsson, H., Futaana, Y., ... Brain, D. A. (2012). A case study of proton precipitation at Mars: Mars Express observations and hybrid simulations. *Journal of Geophysical Research: Space Physics*, *117*(A6). Retrieved 2020-02-18, from `https://agupubs.onlinelibrary.wiley.com/doi/abs/10.1029/2012JA017537` doi: 10.1029/2012JA017537

Diéval, C., Stenberg, G., Nilsson, H., & Barabash, S. (2013). A statistical study of proton precipitation onto the Martian upper atmosphere: Mars Express observations. *J. Geophys. Res.*, *118*, 1972–1983. doi: 10.1002/jgra.50229

Fowler, C. M., Halekas, J., Schwartz, S., Goodrich, K. A., Gruesbeck, J. R., & Benna, M. (2019). The Modulation of Solar Wind Hydrogen Deposition in the Martian Atmosphere by Foreshock Phenomena. *Journal of Geophysical Research: Space Physics*, *124*(8), 7086–7097. Retrieved 2020-02-10, from `https://agupubs.onlinelibrary.wiley.com/doi/abs/10.1029/2019JA026938` (tex.ids: fowlerModulationSolarWind2019a) doi: 10.1029/2019JA026938

Futaana, Y., Barabash, S., Grigoriev, A., Holmström, M., Kallio, E., Brandt, P. C., ... Dierker, C. (2006, June). First ENA observations at Mars: ENA emissions from the martian upper atmosphere. *Icarus*, *182*(2), 424–430. Retrieved 2020-02-10, from `http://www.sciencedirect.com/science/article/pii/S0019103505004707` doi: 10.1016/j.icarus.2005.09.019

Gunell, H., Brinkfeldt, K., Holmström, M., Brandt, P. C., Barabash, S., Kallio, E., ... Dierker, C. (2006, June). First ENA observations at Mars: Charge exchange ENAs produced in the magnetosheath. *Icarus*, *182*(2), 431–438. Retrieved 2020-02-18, from `http://www.sciencedirect.com/science/article/pii/S0019103505004598` doi: 10.1016/j.icarus.2005.10.027

Gunell, H., Holmström, M., Barabash, S., Kallio, E., Janhunen, P., Nagy, A. F., & Ma, Y. (2006, February). Planetary ENA imaging: Effects of different interaction models for Mars. *Planetary and Space Science*, *54*(2), 117–131. Retrieved

2020-02-28, from http://www.sciencedirect.com/science/article/pii/S0032063305000516 doi: 10.1016/j.pss.2005.04.002

Halekas, J. S. (2017, May). Seasonal variability of the hydrogen exosphere of Mars: Mars Hydrogen. *Journal of Geophysical Research: Planets*, *122*(5), 901–911. Retrieved 2019-12-04, from http://doi.wiley.com/10.1002/2017JE005306 doi: 10.1002/2017JE005306

Halekas, J. S., Benna, M., Mahaffy, P. R., Elphic, R. C., Poppe, A. R., & Delory, G. T. (2015, July). Detections of lunar exospheric ions by the LADEE neutral mass spectrometer: LADEE NMS ION DETECTIONS. *Geophysical Research Letters*, *42*(13), 5162–5169. Retrieved 2019-12-04, from http://doi.wiley.com/10.1002/2015GL064746 doi: 10.1002/2015GL064746

Halekas, J. S., Lillis, R. J., Mitchell, D. L., Cravens, T. E., Mazelle, C., Connerney, J. E. P., ... Ruhunusiri, S. (2015). MAVEN observations of solar wind hydrogen deposition in the atmosphere of Mars. *Geophysical Research Letters*, *42*(21), 8901–8909. Retrieved 2019-12-31, from https://agupubs.onlinelibrary.wiley.com/doi/abs/10.1002/2015GL064693 doi: 10.1002/2015GL064693

Halekas, J. S., Ruhunusiri, S., Harada, Y., Collinson, G., Mitchell, D. L., Mazelle, C., ... Jakosky, B. M. (2017, January). Structure, dynamics, and seasonal variability of the Mars-solar wind interaction: MAVEN Solar Wind Ion Analyzer in-flight performance and science results. *Journal of Geophysical Research: Space Physics*, *122*(1), 547–578. Retrieved 2019-12-04, from https://onlinelibrary.wiley.com/doi/abs/10.1002/2016JA023167 doi: 10.1002/2016JA023167

Halekas, J. S., Taylor, E. R., Dalton, G., Johnson, G., Curtis, D. W., McFadden, J. P., ... Jakosky, B. M. (2015). The Solar Wind Ion Analyzer for MAVEN. *Space Sci. Rev.*, *195*, 125–151. doi: 10.1007/s11214-013-0029-z

Hara, T., Luhmann, J. G., Leblanc, F., Curry, S. M., Seki, K., Brain, D. A., ... Jakosky, B. M. (2017). MAVEN observations on a hemispheric asymmetry of precipitating ions toward the Martian upper atmosphere according to the upstream solar wind electric field. *Journal of Geophysical Research: Space Physics*, *122*(1), 1083–1101. Retrieved 2020-04-14, from http://agupubs.onlinelibrary.wiley.com/doi/abs/10.1002/2016JA023348 (_eprint: https://onlinelibrary.wiley.com/doi/pdf/10.1002/2016JA023348) doi: 10.1002/2016JA023348

Henderson, S. (2019). *An Analysis of Precipitating Solar Wind Hydrogen at Mars: Observations by the Maven Spacecraft* (Master's thesis, The University of Iowa, United States – Iowa). Retrieved 2020-08-25, from http://search.proquest.com/docview/2384787388/abstract/7E5C81001AE9403CPQ/1 (ISBN: 9781392759431)

Hughes, A., Chaffin, M., Mierkiewicz, E., Deighan, J., Jain, S., Schneider, N., ... Jakosky, B. (2019). Proton Aurora on Mars: A Dayside Phenomenon Pervasive in Southern Summer. *Journal of Geophysical Research: Space Physics*, *124*(12), 10533–10548. Retrieved 2020-08-14, from http://agupubs.onlinelibrary.wiley.com/doi/abs/10.1029/2019JA027140 (_eprint: https://onlinelibrary.wiley.com/doi/pdf/10.1029/2019JA027140) doi: 10.1029/2019JA027140

Kallio, E., & Barabash, S. (2001). Atmospheric effects of precipitating energetic hydrogen atoms on the Martian atmosphere. *Journal of Geophysical Research: Space Physics*, *106*(A1), 165–177. Retrieved 2020-02-10, from https://agupubs.onlinelibrary.wiley.com/doi/abs/10.1029/2000JA002003 doi: 10.1029/2000JA002003

Kallio, E., Barabash, S., Brinkfeldt, K., Gunell, H., Holmström, M., Futaana, Y., ... Dierker, C. (2006, June). Energetic Neutral Atoms (ENA) at Mars: Properties of the hydrogen atoms produced upstream of the mar-

tian bow shock and implications for ENA sounding technique around non-magnetized planets. *Icarus*, *182*(2), 448–463. Retrieved 2020-01-07, from http://www.sciencedirect.com/science/article/pii/S0019103506000029 doi: 10.1016/j.icarus.2005.12.019

Morschhauser, A., Lesur, V., & Grott, M. (2014, June). A spherical harmonic model of the lithospheric magnetic field of Mars. *Journal of Geophysical Research: Planets*, *119*(6), 1162–1188. Retrieved 2019-12-04, from http://doi.wiley.com/10.1002/2013JE004555 doi: 10.1002/2013JE004555

Mura, A., Orsini, S., Milillo, A., Kallio, E., Galli, A., Barabash, S., ... Sharber, J. R. (2008, May). ENA detection in the dayside of Mars: ASPERA-3 NPD statistical study. *Planetary and Space Science*, *56*(6), 840–845. Retrieved 2020-02-18, from http://www.sciencedirect.com/science/article/pii/S0032063307003881 doi: 10.1016/j.pss.2007.12.013

Ritter, B., Gérard, J.-C., Hubert, B., Rodriguez, L., & Montmessin, F. (2018, January). Observations of the Proton Aurora on Mars With SPICAM on Board Mars Express. *Geophysical Research Letters*, *45*(2), 612–619. Retrieved 2019-12-04, from http://doi.wiley.com/10.1002/2017GL076235 (tex.ids: ritterObservationsProtonAurora2018a) doi: 10.1002/2017GL076235

Ross, E., & Chaplin, W. J. (2019, January). The Behaviour of Galactic Cosmic-Ray Intensity During Solar Activity Cycle 24. *Solar Physics*, *294*(1), 8. Retrieved 2020-07-17, from https://doi.org/10.1007/s11207-019-1397-7 doi: 10.1007/s11207-019-1397-7

Shematovich, V. I., Bisikalo, D. V., Diéval, C., Barabash, S., Stenberg, G., Nilsson, H., ... Gérard, J.-C. (2011). Proton and hydrogen atom transport in the Martian upper atmosphere with an induced magnetic field. *Journal of Geophysical Research: Space Physics*, *116*(A11). Retrieved 2020-02-18, from https://agupubs.onlinelibrary.wiley.com/doi/abs/10.1029/2011JA017007 doi: 10.1029/2011JA017007

Wang, X.-D., Alho, M., Jarvinen, R., Kallio, E., Barabash, S., & Futaana, Y. (2018). Precipitation of Hydrogen Energetic Neutral Atoms at the Upper Atmosphere of Mars. *Journal of Geophysical Research: Space Physics*, *123*(10), 8730–8748. Retrieved 2020-02-10, from https://agupubs.onlinelibrary.wiley.com/doi/abs/10.1029/2018JA025188 doi: 10.1029/2018JA025188

Wang, X.-D., Barabash, S., Futaana, Y., Grigoriev, A., & Wurz, P. (2013). Directionality and variability of energetic neutral hydrogen fluxes observed by Mars Express. *Journal of Geophysical Research: Space Physics*, *118*(12), 7635–7642. Retrieved 2020-02-10, from https://agupubs.onlinelibrary.wiley.com/doi/abs/10.1002/2013JA018876 doi: 10.1002/2013JA018876

Wang, X.-D., Barabash, S., Futaana, Y., Grigoriev, A., & Wurz, P. (2014). Influence of Martian crustal magnetic anomalies on the emission of energetic neutral hydrogen atoms. *Journal of Geophysical Research: Space Physics*, *119*(10), 8600–8609. Retrieved 2020-02-18, from https://agupubs.onlinelibrary.wiley.com/doi/abs/10.1002/2014JA020307 doi: 10.1002/2014JA020307